


# SCIENTIFIC REPORTS

OPEN

## Anomalous in-plane anisotropic Raman response of monoclinic semimetal $1T'$ -MoTe<sub>2</sub>

Qingjun Song<sup>1,2</sup>, Haifeng Wang<sup>3,4</sup>, Xingchen Pan<sup>3,4</sup>, Xiaolong Xu<sup>1,2</sup>, Yilun Wang<sup>1,2</sup>, Yanping Li<sup>1</sup>, Fengqi Song<sup>3,4</sup>, Xiangang Wan<sup>3,4</sup>, Yu Ye<sup>1,2</sup>  & Lun Dai<sup>1,2</sup>

The recently discovered two-dimensional (2D) semimetal  $1T'$ -MoTe<sub>2</sub> exhibits colossal magnetoresistance and superconductivity, driving a strong research interest in the material's quantum phenomena. Unlike the typical hexagonal structure found in many 2D materials, the  $1T'$ -MoTe<sub>2</sub> lattice has strong in-plane anisotropy. A full understanding of the anisotropy is necessary for the fabrication of future devices which may exploit these quantum and topological properties, yet a detailed study of the material's anisotropy is currently lacking. While angle resolved Raman spectroscopy has been used to study anisotropic 2D materials, such as black phosphorus, there has been no in-depth study of the Raman dependence of  $1T'$ -MoTe<sub>2</sub> on different layer numbers and excitation energies. Here, our angle resolved Raman spectroscopy shows intricate Raman anisotropy dependences of  $1T'$ -MoTe<sub>2</sub> on polarization, flake thickness (from single layer to bulk), photon, and phonon energies. Using a Paczek approximation, the anisotropic Raman response can be captured in a classical framework. Quantum mechanically, first-principle calculations and group theory reveal that the anisotropic electron-photon and electron-phonon interactions are nontrivial in the observed responses. This study is a crucial step to enable potential applications of  $1T'$ -MoTe<sub>2</sub> in novel electronic and optoelectronic devices where the anisotropic properties might be utilized for increased functionality and performance.

Transition metal dichalcogenides (TMDCs) are two-dimensional (2D) materials that have emerged as appealing material systems due to their variable electrical band gap and strong spin-orbit coupling. In addition, a rich and diverse amount of physical phenomena have been realized, from correlated charge density waves and superconductivities, to device-driven transistors, sensors, spintronics, and valley-optoelectronics<sup>1–5</sup>. Recently, 2D materials with lower symmetry have attracted increased attention, due to the significant in-plane anisotropy in their electrical, optical and thermal properties<sup>6–12</sup>. For example, the reduced symmetry of black phosphorus has resulted in the in-plane anisotropic mobility, absorption, and thermal conductivity<sup>6–8</sup>. Whereas many TMDCs are in the 2H phase and are semiconducting, monoclinic  $1T'$ -MoTe<sub>2</sub> is semi-metallic<sup>13</sup>. By decreasing the temperature, the monoclinic  $1T'$  crystal phase changes to the orthorhombic Td phase, resulting in observations of huge magnetoresistance, type-II Weyl semimetal Fermi arcs, and potentially providing a route towards the quantum spin Hall effect<sup>14–21</sup>. Both 2H and monoclinic  $1T'$ -MoTe<sub>2</sub> are stable at room temperature, and the few-layer crystals can be obtained through the chemical vapor deposition method or mechanical exfoliation<sup>22,23</sup>. However, the studies regarding monoclinic 2D materials and their anisotropic properties are still limited, which is a crucially necessary for the future design and realization of devices with emergent quantum and topological properties for enhanced performance.

Raman spectroscopy is a conventional and non-destructive technique for the characterization of the crystal structure<sup>24</sup>. In 2D materials, Raman spectroscopy is a powerful tool that is typically used to determine the number of layers and provide insight into the doping, strain, and crystal phases<sup>25–29</sup>. Thus, the angle resolved polarized Raman response of monoclinic  $1T'$ -MoTe<sub>2</sub> can reveal the material's anisotropic light-matter interaction, necessary for the improved design of electronic, thermoelectric and optoelectronic devices<sup>30</sup>. Here, we study the

<sup>1</sup>State Key Lab for Mesoscopic Physics and School of Physics, Peking University, Beijing, 100871, China.

<sup>2</sup>Collaborative Innovation Center of Quantum Matter, Beijing, 100871, China. <sup>3</sup>National Laboratory of Solid State Microstructures, College of Physics, Nanjing University, Nanjing, 210093, China. <sup>4</sup>Collaborative Innovation Center of Advanced Microstructures, Nanjing University, Nanjing, 210093, China. Correspondence and requests for materials should be addressed to X.W. (email: [xgwan@nju.edu.cn](mailto:xgwan@nju.edu.cn)) or Y.Y. (email: [ye\\_yu@pku.edu.cn](mailto:ye_yu@pku.edu.cn)) or L.D. (email: [lundai@pku.edu.cn](mailto:lundai@pku.edu.cn))

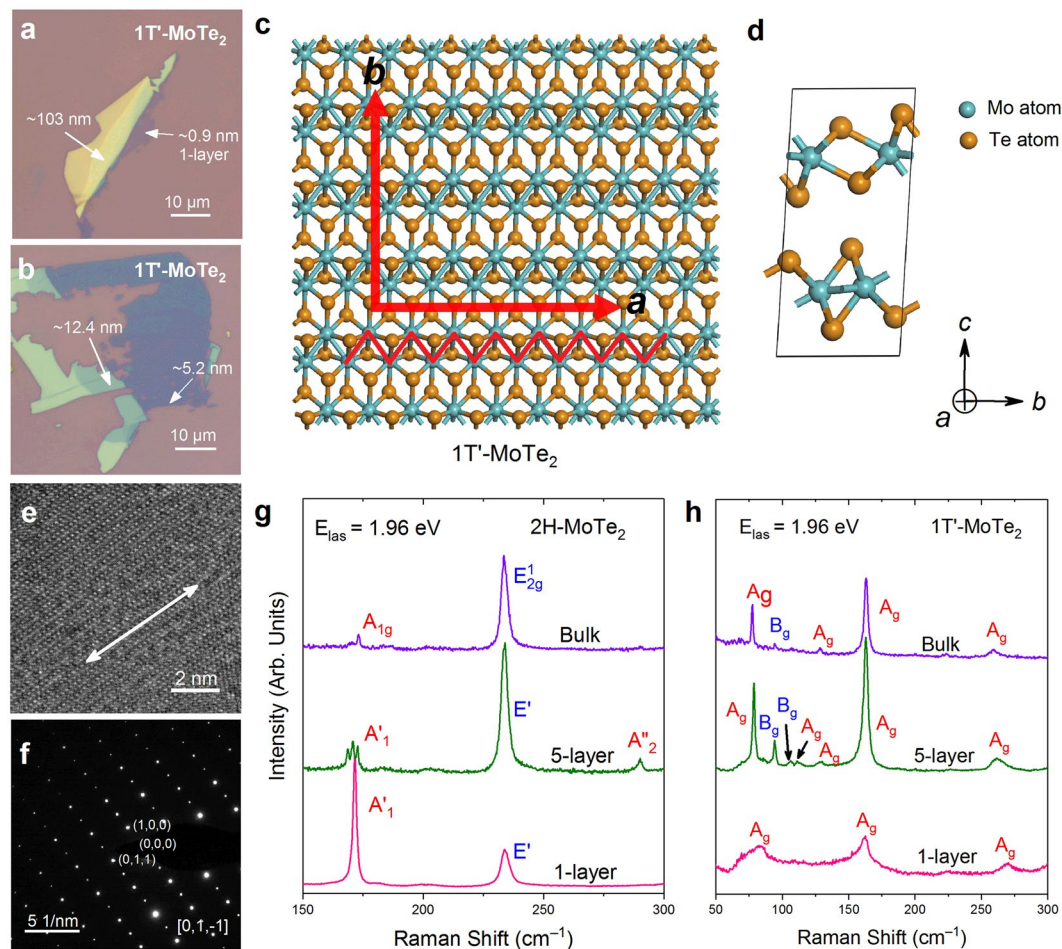


**Figure 1.** (a,b) The optical images of exfoliated single-layer and few-layer  $1T'$ - $\text{MoTe}_2$  on a 285 nm  $\text{SiO}_2/\text{Si}$  substrates. The thicknesses of the flakes are labeled. (c) The top view crystal structure of single-layer  $1T'$ - $\text{MoTe}_2$ . The zigzag metal chains,  $a$ -axis and  $b$ -axis are labeled. (d) The side view unit cells of  $1T'$ - $\text{MoTe}_2$ . (e) The high-resolution TEM image of few-layer  $1T'$ - $\text{MoTe}_2$ , where the direction of Mo-Mo chain is represented by a white double-headed arrow. (f) The selected electron diffraction image of  $1T'$ - $\text{MoTe}_2$  flakes top-viewed from the  $[01-1]$  zone. (g,h) The representative  $1T'$ - $\text{MoTe}_2$  and  $2H$ - $\text{MoTe}_2$  Raman spectra of 1-layer, 5-layer, and bulk.

anisotropic Raman response of monoclinic  $1T'$ - $\text{MoTe}_2$  from single layer to bulk using two different measurement methods. By rotating the sample, the symmetries of the detected modes can be identified through their periods of intensity variation. This method allows us to easily and rapidly identify the crystalline orientation of  $1T'$ - $\text{MoTe}_2$  using the  $A_g$  ( $A'$ ) modes with maximum Raman intensities. In addition, the anisotropic Raman response's dependence on the  $1T'$ - $\text{MoTe}_2$  thickness and photon excitation wavelength are carried out by rotating the incident light polarization method, while fixing the sample orientation and scattered light polarization. Using this method, the polar plots of the intensities for all detected modes exhibit a two-lobed shape, while the main-axis orientations for different symmetric modes are different. Their polarization-dependent intensities roughly coincide with the semi-classical model based on the Placzek approximation. Using the full quantum model based on the density functional and quantum perturbation theories, we demonstrate that the anisotropy of Raman modes is both influenced by the anisotropic electron-photon interaction and the anisotropic electron-phonon interaction. Our research not only explores the in-plane anisotropic intensities of Raman modes in monoclinic  $2D$   $1T'$ - $\text{MoTe}_2$ , but also reveals the physical origin of the anisotropic Raman response, beneficial for the design of future devices which utilize the anisotropic optical, electrical, and mechanical properties of TMDCs<sup>30</sup>.

## Results and Discussions

**Raman Spectra of  $1T'$ - $\text{MoTe}_2$ .** The single-layer and few-layer  $1T'$ - $\text{MoTe}_2$  were mechanically exfoliated from  $1T'$ - $\text{MoTe}_2$  crystals (more details in Methods)<sup>14,20</sup> onto a 285 nm  $\text{SiO}_2/\text{Si}$  substrate (Fig. 1a–b). Their layer numbers were first identified by optical contrast and then confirmed by atomic force microscopy (AFM). In  $1T'$ - $\text{MoTe}_2$ , the formation of in-plane Mo-Mo bonds lead to a pseudo-hexagonal layer with zigzag metal chains (Fig. 1c). The layer stacking in  $1T'$ - $\text{MoTe}_2$  is slightly tilted with  $\beta = 93.4^\circ$  in a monoclinic fashion, resulting in the low symmetry (Fig. 1d). In order to obtain the details of the crystal structure, the exfoliated  $1T'$ - $\text{MoTe}_2$  flakes are transferred to a micro-grid for high-resolution transmission electron microscopy (HR-TEM). The HR-TEM image displays a distinct one-dimensional chain (Fig. 1e), which corresponds to the crystalline direction of the

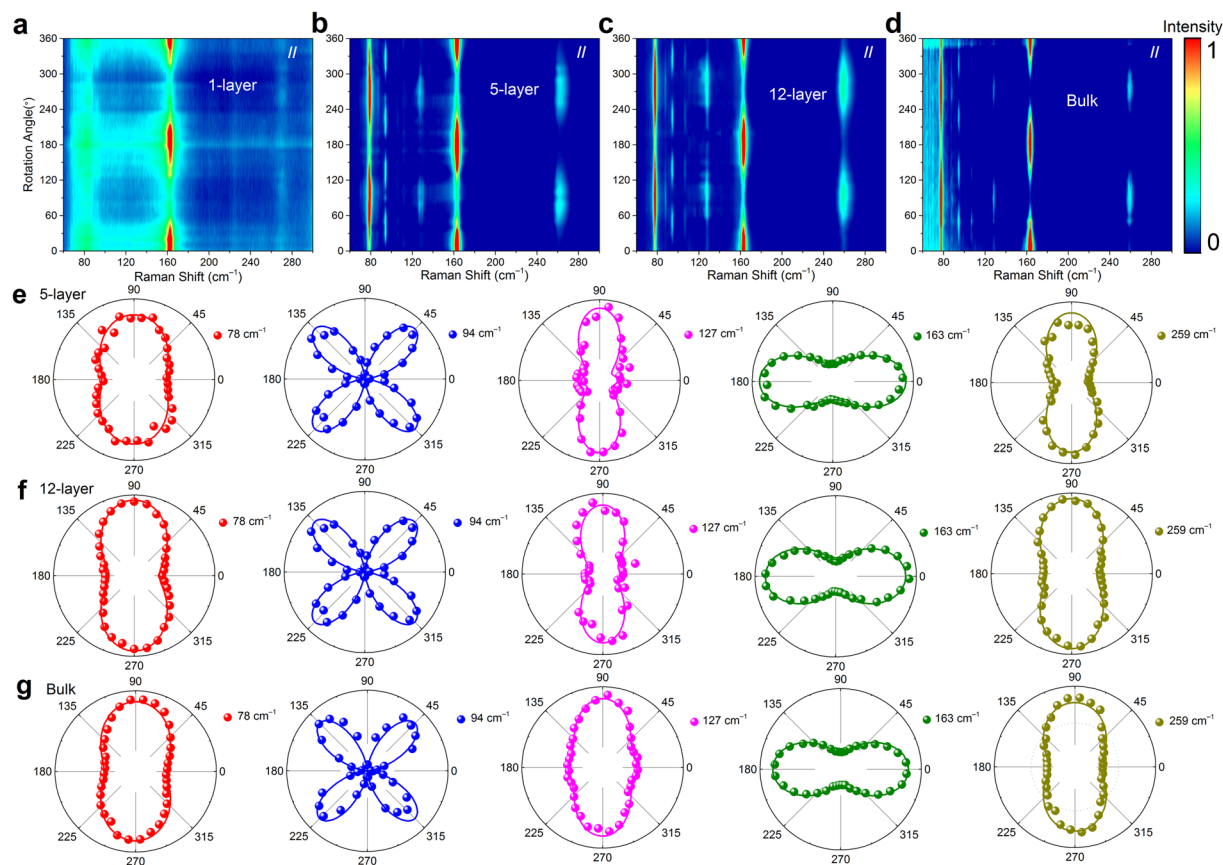


**Figure 2.** The sample rotation angle dependent Raman spectra of (a) 1-layer, (b) 5-layer, (c) 12-layer and (d) bulk  $1T'$ -MoTe<sub>2</sub> in the parallel polarization configuration. The polar plots of the angle-dependent intensities of phonon modes in (e) 5-layer, (f) 12-layer and (g) bulk  $1T'$ -MoTe<sub>2</sub>. The initial angle is set when the crystalline  $a$ -axis is parallel to the incident polarization.

$a$ -axis. Furthermore, the selected area electron diffraction (SAED) pattern (Fig. 1f) confirms the clear monoclinic symmetry.

The representative Raman spectra of 1-layer, 5-layer, bulk MoTe<sub>2</sub> in both the  $1T'$  and 2H (2D Semiconductors) phase are measured (Fig. 1g–h) using an excitation energy of 1.96 eV. The only modes observed in single-layer and bulk 2H-MoTe<sub>2</sub> are the  $A_1'$  ( $\sim 172$  cm<sup>-1</sup>) and  $E'$  ( $\sim 233$  cm<sup>-1</sup>) modes. In 5-layer 2H-MoTe<sub>2</sub>, apart from the corresponding  $A_1'$  and  $E'$  modes, an  $A_2''$  ( $\sim 291$  cm<sup>-1</sup>) mode, originates from the interlayer interactions under the 2D limit, can be detected. In addition, three Davydov components of the  $A_1'$  modes in 5-layer, which originates from the in-phase and out-of-phase interlayer interactions<sup>25,26</sup>, are clearly observed. In contrast, several peaks at lower wave numbers are observed in  $1T'$ -MoTe<sub>2</sub>. For single-layer  $1T'$ -MoTe<sub>2</sub>, only three modes ( $\sim 83$ , 165, 270 cm<sup>-1</sup>) can be observed. However, in 5-layer and bulk  $1T'$ -MoTe<sub>2</sub>, the number of detected modes increases. Given the same layer number, the number of detected modes in  $1T'$ -MoTe<sub>2</sub> is greater than that in 2H-MoTe<sub>2</sub>, reflecting the lower crystal symmetry of the  $1T'$  phase compared with the 2H phase<sup>31</sup>.

**In-plane Anisotropic Raman Response by Rotating Sample.** The angle-resolved Raman spectroscopy of 2D materials' in-plane anisotropy can be carried out by rotating the sample or incident light polarization (more details in Methods)<sup>11,30</sup>. The rotating sample method was used to study the symmetry of these detected modes and identify crystalline orientation of the exfoliated flakes<sup>10–12</sup>. In this measurement, an analyzer was placed before the entrance of the spectrometer, allowing for the analysis of scattered Raman signal polarized parallel or perpendicular to the incident light polarization (parallel- or cross-polarization configurations, respectively). Raman spectra of 1-layer, 5-layer, 12-layer and bulk  $1T'$ -MoTe<sub>2</sub> in the parallel-polarization configuration (Fig. 2a–d) exhibit strong rotation angle dependence. Only two modes could be clearly observed in single-layer  $1T'$ -MoTe<sub>2</sub> in the range of 50–300 cm<sup>-1</sup>, due to the absence of interlayer coupling. Both modes show obvious 180° periodic variations with the sample rotation angle, yielding a two-lobed shape with two maximum intensity angles (Fig. 2a). The mode at 270 cm<sup>-1</sup> is too weak to show a clear angle dependence. In 5-layer, 12-layer and bulk  $1T'$ -MoTe<sub>2</sub>, more Raman modes are detected (Fig. 2b–d). Some modes depict 180° periodic variations yielding two-lobed shapes in their polar plots (Fig. 2e–g), while others depict 90° periodic variations yielding four-lobed shapes in corresponding polar plots (Fig. 2e–g).

The angle dependences of five representative Raman modes ( $\sim 78$ , 94, 127, 163 and 259 cm<sup>-1</sup>) in 5-layer, 12-layer and bulk  $1T'$ -MoTe<sub>2</sub> are shown in Fig. 2e–g, respectively. The modes at  $\sim 78$ , 127, 163, and 259 cm<sup>-1</sup>

		78 cm <sup>-1</sup>	127 cm <sup>-1</sup>	163 cm <sup>-1</sup>	259 cm <sup>-1</sup>
5-layer	a/b	~1.40	~2.00	~0.50	~2.02
	cosϕ <sub>ba</sub>	~1.00	~0.10	~0.60	~0.70
12-layer	a/b	~1.73	~2.01	~0.49	~1.74
	cosϕ <sub>ba</sub>	~1.00	~0.30	~0.94	~0.90
bulk	a/b	~1.48	~1.41	~0.49	~1.58
	cosϕ <sub>ba</sub>	~1.00	~0.60	~0.94	~0.98

**Table 1.** The fitted values of |a/b| and phase difference ϕ<sub>ba</sub> for the detected A<sub>g</sub> (A') modes in 5-layer, 12-layer and bulk 1 T'-MoTe<sub>2</sub>.

show obvious 180° periodic intensity variations, while the mode at ~94 cm<sup>-1</sup> shows a 90° period. The main-axis of the two-lobed shapes at ~78, 127, and 259 cm<sup>-1</sup> is perpendicular to the one-dimensional (1D) Mo-Mo chain (*a*-axis). However, the mode at ~163 cm<sup>-1</sup> depicts a two-lobed shape with the main-axis parallel to the *a*-axis. In other words, the mode at ~163 cm<sup>-1</sup> reaches its maximum intensity when the polarization of incident laser is along the well-defined Mo-Mo zigzag metal chain of the flakes. We have extensively measured more than twenty flakes with different thicknesses, and verified that the polarized angle dependence of ~163 cm<sup>-1</sup> mode can be used to identify the crystalline orientation of 1 T'-MoTe<sub>2</sub> flakes. The two-lobed modes can be further classified into two categories: the modes with maximum Raman intensity along or perpendicular to the 1D Mo-Mo chains under parallel polarization. These angle-dependent Raman intensities can be quantitatively understood based on the semi-classical analysis, which can be expressed as:<sup>10</sup>

$$I \propto |e_i \cdot \tilde{R} \cdot e_s|^2 \quad (1)$$

where both the incident and scattered light polarization unitary vectors, *e<sub>i</sub>* and *e<sub>s</sub>*, are (cosθ, sinθ, 0) in the parallel polarization configuration, θ is the angle between the incident laser polarization and the 1D Mo-Mo chain (*a*-axis), and  $\tilde{R}$  is the Raman tensor for the Raman active modes of 1 T'-MoTe<sub>2</sub>. Bulk and odd numbered 1 T'-MoTe<sub>2</sub> flakes belong to the space group *P2<sub>1</sub>/m* and point group *C<sub>2h</sub><sup>2</sup>*, with 12 atoms and 6*N* atoms in the unit cell, respectively. The irreducible representations for all possible phonon modes at the Brillion zone center  $\Gamma$  point in bulk and odd numbered 1 T'-MoTe<sub>2</sub> can be written as  $\Gamma_{\text{bulk}} = 12A_g + 6A_u + 6B_g + 12B_u$  and  $\Gamma_{\text{odd}} = 6N A_g + 3N A_u + 3N B_g + 6N B_u$ , where *N* presents the number of layers. Even numbered 1 T'-MoTe<sub>2</sub> flakes belong to the space group *Pm* and point group *C<sub>s</sub><sup>1</sup>*. The irreducible representations of possible phonon modes at  $\Gamma$  point in *N*-layer 1 T'-MoTe<sub>2</sub> can be written as  $\Gamma_{\text{even}} = 6N A' + 12N A''$ . Among them, A<sub>g</sub> and B<sub>g</sub> are Raman active, A<sub>u</sub> and B<sub>u</sub> are infrared active, while A' and A'' are both Raman and infrared active. It is worth noting that, in an absorptive material, the elements of the Raman tensors should be complex numbers, with real and imaginary parts<sup>10</sup>.

$$\tilde{R}(A_g/A') = \begin{pmatrix} |a|e^{i\phi_a} & 0 & |d|e^{i\phi_d} \\ 0 & |b|e^{i\phi_b} & 0 \\ |d|e^{i\phi_d} & 0 & |c|e^{i\phi_c} \end{pmatrix}$$

$$\tilde{R}(B_g/A'') = \begin{pmatrix} 0 & |e|e^{i\phi_e} & 0 \\ |e|e^{i\phi_e} & 0 & |f|e^{i\phi_f} \\ 0 & |f|e^{i\phi_f} & 0 \end{pmatrix}$$

Here, ϕ represents the phase of the corresponding tensor element<sup>10,30</sup>. A phonon mode can only be detected when  $|e_i \cdot \tilde{R} \cdot e_s|^2$  has non-zero value. Therefore, using parallel polarization, the above defined unitary vectors (*e<sub>i</sub>* and *e<sub>s</sub>*), as well as the Raman tensors of the A<sub>g</sub> (A') and B<sub>g</sub> (A'') modes, we can obtain their angular dependent Raman intensity expressions:

$$I_{A_g(A')}^{\parallel} \propto |a|^2 \left[ \left( \frac{|b|}{|a|} \sin^2\theta + \cos^2\theta \cos\phi_{ba} \right)^2 + \cos^4\theta \sin^2\phi_{ba} \right] \quad (2)$$

$$I_{B_g(A'')}^{\parallel} \propto |e|^2 \sin^2 2\theta \quad (3)$$

where ϕ<sub>ba</sub> is the phase difference ϕ<sub>b</sub>-ϕ<sub>a</sub>. The experimental angle-dependent Raman intensities of the detected modes can be fitted by the equations (2) and (3) (Fig. 2e-f), yielding the corresponding ϕ<sub>ba</sub> and |b/a| for A<sub>g</sub> (A') modes, summarized in Table 1. According to the above two equations, the modes with 180° periodic intensity variation (~78, 127, 163 and 259 cm<sup>-1</sup>) belong to A<sub>g</sub> (A') modes for odd- (even-) numbered 1 T'-MoTe<sub>2</sub>, while the ones with the 90° periodic intensity variation (94 and 115 cm<sup>-1</sup>) belong to B<sub>g</sub> (A'') mode for odd- (even-) numbered 1 T'-MoTe<sub>2</sub>. It is worth noting that the mode at ~163 cm<sup>-1</sup> is not the B<sub>g</sub> mode as assigned in ref.<sup>22</sup>, because the intensity variation period is 180° (two-lobed shape), not 90° (four-lobed shape) in the parallel polarization

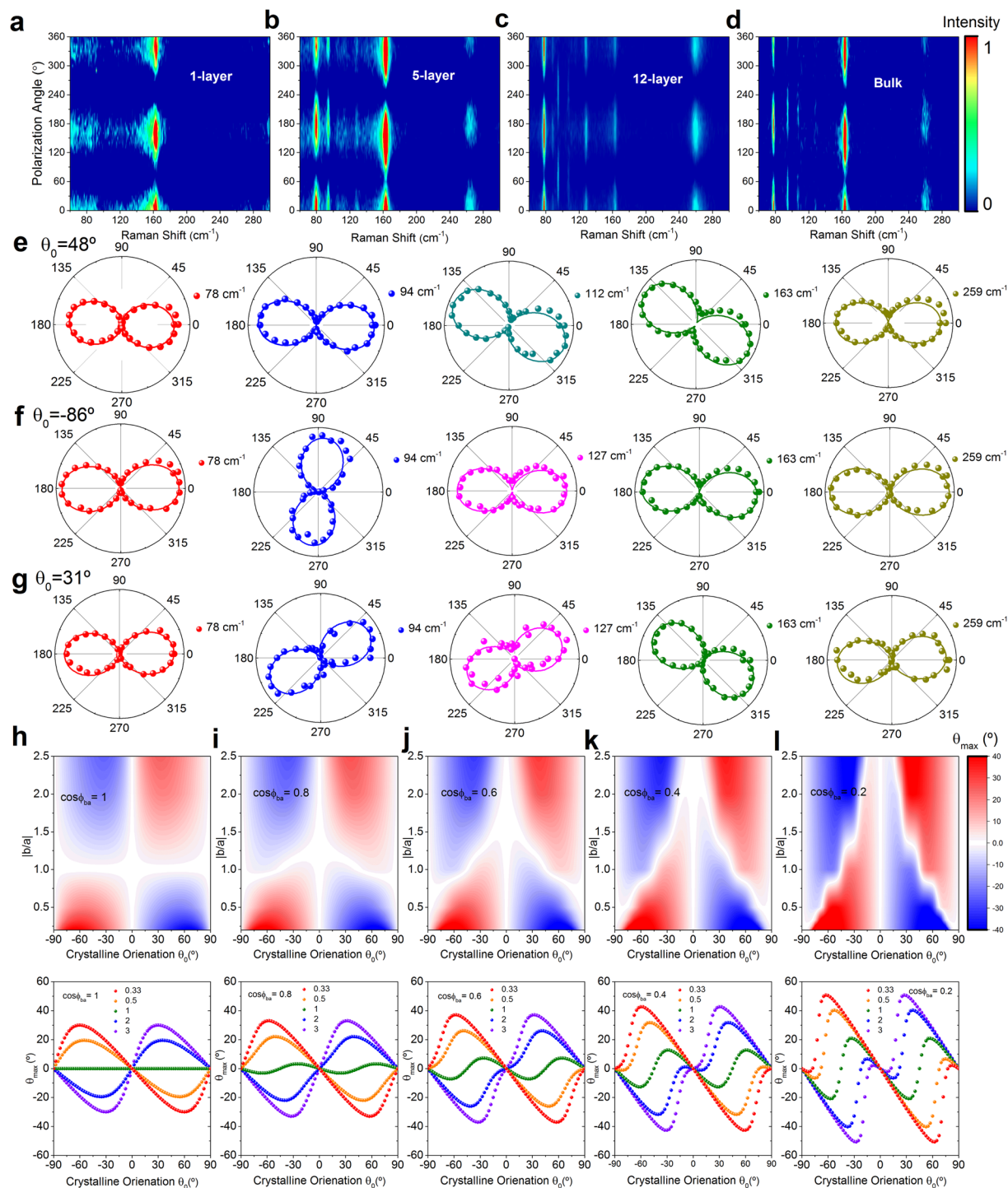


**Figure 3.** The rotation of the incident laser polarization dependent Raman spectra of (a) 1-layer, (b) 5-layer, (c) 12-layer and (d) bulk 1T'-MoTe<sub>2</sub>, the initial incident polarization is parallel to the scattered polarization. Each spectrum has been normalized to its maximum intensity, respectively. The polar plots of the three detected mode types for (e) 5-layer, (f) 12-layer and (g) bulk 1T'-MoTe<sub>2</sub> samples. The calculated  $\theta_{\max}$  as a function of  $\theta_0$  and  $|b/a|$ , where the value of  $\cos \phi_{ba}$  is (h) 1, (i) 0.8, (j) 0.6, (k) 0.4, and (l) 0.2. The corresponding relation between  $\theta_{\max}$  and  $\theta_0$  with certain  $|b/a|$  (0.33, 0.5, 1, 2 and 3) is plotted below each panel.

configuration. According to equation (2), the  $A_g$  ( $A'$ ) modes can also be classified into two types according to the Raman tensor element values  $|a| < |b|$  or  $|a| > |b|$ . Type I  $A_g$  ( $A'$ ) modes ( $\sim 78, 127$  and  $259 \text{ cm}^{-1}$ ) with  $|a| < |b|$  result in a main-axis of the two-lobed shape perpendicular to the  $a$ -axis, while type II  $A_g$  ( $A'$ ) modes ( $\sim 163 \text{ cm}^{-1}$ ) with  $|a| > |b|$  result in a main-axis of the two-lobed shape parallel to the  $a$ -axis. Therefore, the angle-dependent Raman

spectroscopy in the parallel-polarized configuration provides an all-optical method for the identification of crystal orientation and can be used to determine the Raman modes' symmetry in 1T'-MoTe<sub>2</sub>.

**In-plane Anisotropic Raman Response by Rotating Incident Polarization.** In order to further study the anisotropic Raman response of 1T'-MoTe<sub>2</sub>, we carried out angle-dependent polarized Raman spectroscopy by rotating the incident laser polarization while fixing the sample and scattered light polarization. In the measurement, a half-wave plate was placed after the incident polarizer, allowing for the analysis of the scattered Raman signals with the incident laser polarization rotation angle of  $\theta$ , while the half-wave plate was rotated by an angle of  $\theta/2$ . Compared with the sample rotation method, the incident polarization rotation method is more convenient, as the half-wave plate rotation is programmable. At first, the incident laser polarization is set parallel to the scattered light polarization, and the angle between the scattered light polarization and the crystalline  $a$ -axis (obtained through the anisotropic Raman spectra in the parallel polarization configuration) is  $\theta_0$ . If the direction of the crystalline  $a$ -axis is clockwise compared with the scattered light polarization, the  $\theta_0$  is positive, otherwise negative. The representative incident polarization dependent Raman spectra of 1-layer, 5-layer, 12-layer, and bulk MoTe<sub>2</sub> were measured under the excitation energy of 1.96 eV (Fig. 3a–d). We can see that all the detected Raman modes (classified above) depict a two-lobed shape, but the main-axes are not simply parallel or perpendicular to the crystal  $a$ -axis (Fig. 3e–g). Considering the crystal symmetry and complex form of the Raman tensors, the above anisotropic results can be understood based on the semi-classical analysis, where the unit vectors of the incident and scattered light polarization are identical and can be expressed as  $(\cos(\theta + \theta_0), \sin(\theta + \theta_0), 0)$  and  $(\cos\theta_0, \sin\theta_0, 0)$ . The angular dependent Raman intensity of  $A_g (A')$  and  $B_g (A'')$  modes can be written as:

$$I_{A_g (A')} \propto |a|^2 \cos^2(\theta + \theta_0) \cos^2\theta_0 + |b|^2 \sin^2(\theta + \theta_0) \sin^2\theta_0 + \frac{1}{2}|a||b| \sin[2(\theta + \theta_0)] \sin 2\theta_0 \cos\phi_{ba} \quad (4)$$

$$I_{B_g (A'')} \propto |e|^2 \sin^2(\theta + 2\theta_0) \quad (5)$$

We can see that the intensity variation periods for all these modes are 180°. The main-axis orientation of the two-lobed shape is represented by the angle of the incident polarization with the maximum Raman intensity,  $\theta_{\max}$ . From equation (4),  $\theta_{\max}$  of an  $A_g (A')$  phonon mode should meet conditions where the first-order derivative is zero while the second-order derivative is negative:

$$(|b/a|^2 \sin^2\theta_0 - \cos^2\theta_0) \sin[2(\theta_0 + \theta_{\max})] + |b/a| \cos[2(\theta_0 + \theta_{\max})] \sin 2\theta_0 \cos\phi_{ba} = 0 \quad (6)$$

and

$$(|b/a|^2 \sin^2\theta_0 - \cos^2\theta_0) \cos[2(\theta_0 + \theta_{\max})] - |b/a| \sin[2(\theta_0 + \theta_{\max})] \sin 2\theta_0 \cos\phi_{ba} < 0 \quad (7)$$

Similarly,  $\theta_{\max}$  of a  $B_g (A'')$  mode should meet:

$$2\theta_0 + \theta_{\max} = \pm 90^\circ \quad (8)$$

The values of  $\theta_0$  and  $\theta_{\max}$  are set in the range of  $-90^\circ$  to  $90^\circ$ . The  $\theta_{\max}$  is a function of  $\theta_0$  and Raman tensor element ratio  $|b/a|$  (Fig. 3h–l). When the initial incident polarization is parallel to the crystal  $a$ -axis ( $\theta_0 = 0$ ), the value of  $\theta_{\max}$  is zero. We can see that  $\theta_{\max}$  has an enhanced variation with  $\theta_0$  when the Raman tensor element  $|b|$  deviates from  $|a|$ . This phenomenon can be clearly seen in Fig. 3h–l with  $|b/a|$  of 0.33, 0.5, 1, 2, and 3, respectively. For an absorptive material, the phase difference,  $\phi_b - \phi_a$ , will change the dispersion of  $\theta_{\max}$ . Figure 3h–l displays the evolution of the  $\theta_{\max}$  dispersion with an increased phase difference, represented by  $\cos\phi_{ba}$  values of 1, 0.8, 0.6, 0.4, and 0.2, respectively. Based on the above calculation, combined with the experimental extracted  $|b/a|$  values, the experimental  $\theta_{\max}$  of the  $A_g (A')$  mode varies from about  $-40^\circ$  to  $40^\circ$ , in good agreement with experimental observations. With the incident polarization rotation method, the above analysis demonstrates the main-axis orientation of the two-lobed  $A_g (A')$  mode is not simply parallel or perpendicular to the crystal  $a$ -axis, but is a function of crystal orientation  $\theta_0$ ,  $|b/a|$ , and the phase difference  $\phi_{ba}$ .

**Excitation Energy Dependence.** The number of detected modes in few-layer 1T'-MoTe<sub>2</sub> is limited compared with that in Td-WTe<sub>2</sub><sup>12</sup>. In order to detect more modes and further study the Raman response of 1T'-MoTe<sub>2</sub> on polarization, phonon and photon energies, we carried out the anisotropic Raman measurements with three additional excitation energies (1.83, 2.28, and 2.54 eV) via rotating the incident polarization. The 12-layer 1T'-MoTe<sub>2</sub> flake with  $\theta_0 = -86^\circ$  was chosen as the representative sample, due to the considerable number and intensity of the detectable modes as well as the easily identifiable mode symmetry. Figure 4a–c shows the polarization-dependent Raman spectra of 12-layer 1T'-MoTe<sub>2</sub> under these three excitation energies, respectively. A total of 8 modes can be resolved with an excitation energy of 2.28 eV, while some modes are missing with an excitation energy of 1.83 and 2.54 eV. We calculated the phonon dispersion curve of bulk 1T'-MoTe<sub>2</sub> (Fig. 4d) using density functional theory (DFT) and found all 36 normal modes at the Brillouin zone center  $\Gamma$  point are non-degenerate in bulk 1T'-MoTe<sub>2</sub>, which differs from that of 2H-type TMDCs with higher symmetry (the modes vibrating parallel to the 2D plane are double degenerate). The measured Raman frequencies and identified mode symmetries agree well with the calculated phonon modes from DFT (Fig. 4e). The atomic displacements for the lattice vibration of detected modes and their polarization-dependent intensities using excitation energies of 1.83, 2.28, and 2.54 eV are shown in Fig. 4e–h, respectively. Based on equations (6–8), for a  $\theta_0$  of  $-86^\circ$  (closer to  $-90^\circ$ ), the main-axis orientation  $\theta_{\max}$  of  $A_g (A')$  mode is closer to zero, and that of  $B_g (A'')$  mode is closer to  $\pm 90^\circ$ .

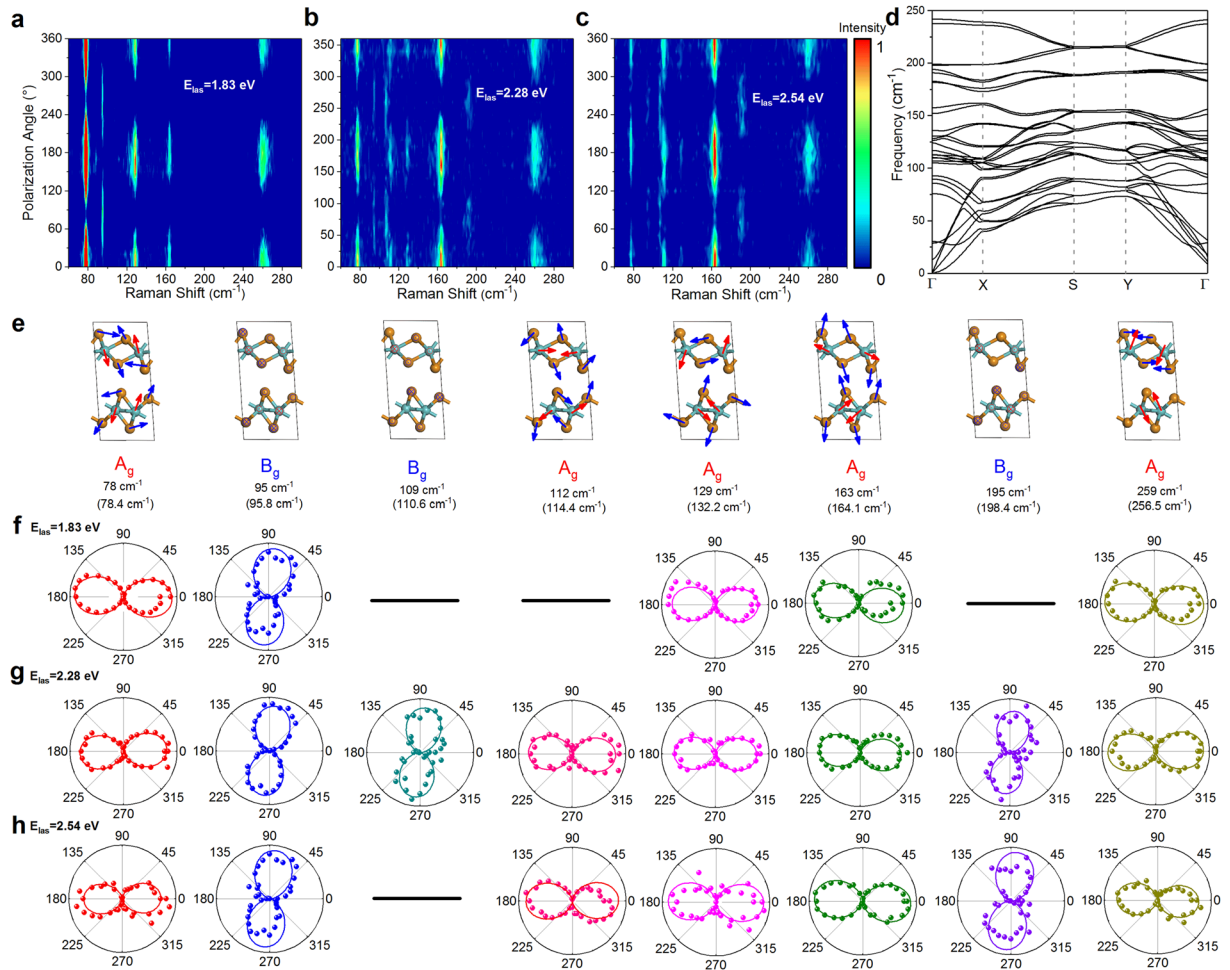


**Figure 4.** The incident laser polarization dependent Raman spectra of a 12-layer 1T'-MoTe<sub>2</sub> using an excitation energy of (a) 1.83, (b) 2.28 and (c) 2.54 eV. The initial incident polarization is parallel to the scattered polarization, and  $\theta_0 = -86^\circ$ . Each spectrum has been normalized to its maximum intensity, respectively. (d) Calculated phonon dispersion curves of 1T'-MoTe<sub>2</sub> bulk along the  $\Gamma$ -X-S-Y- $\Gamma$  direction in the Brillouin zone. (e) The calculated atomic displacements for the lattice vibrations of the ten detected modes in 1T'-MoTe<sub>2</sub>, together with their corresponding irreducible representations. The theoretical frequency is given below in each panel. The atomic displacements of Mo (Te) atoms are shown in red (blue) arrows. The Raman intensities were given as polar plots of the detected modes with an excitation energy of (f) 1.83, (g) 2.28 and (h) 2.54 eV.

Then the modes at 78, 112, 127, 163 and 259  $\text{cm}^{-1}$  are  $A_g$  ( $A'$ ) modes, while the ones at 95, 109, and 195  $\text{cm}^{-1}$  are  $B_g$  ( $A''$ ) modes. The measured Raman frequencies and mode symmetries agree well with those of the DFT calculated phonon modes (Fig. 4e–h and supplementary Table S1). The atoms of the  $B_g$  ( $A''$ ) modes vibrate along the Mo-Mo zigzag chain, while the atoms of the  $A_g$  ( $A'$ ) modes vibrate within the mirror plane perpendicular to the chain. We conclude that 2.28 eV is an appropriate excitation energy to detect more Raman modes in few-layer 1T'-MoTe<sub>2</sub>, and the symmetry of detected modes can be easily identified in the incident polarization rotation method.

**Full Quantum Model of Anisotropic Raman Response.** To further explore the physical origin of the anisotropic Raman response, we employed the full quantum model based on DFT calculation and quantum perturbation theory<sup>28</sup>. The Raman scattering response contains three processes: incident photon absorption, the creation/destruction of the phonon, and scattered photon emission. The incident photon absorption and scattered photon emission processes are related to the electron-photon interactions, while the creation/destruction of the phonon is related to the electron-phonon interaction. The Raman intensity with incident laser photon energy ( $E_{las}$ ) can be obtained by incorporating two electron-photon matrix elements and one electron-phonon matrix element as follows:

$$I(E_{las}) = \left| \sum_{i,m,n} \frac{\langle f|H_{e-p}|n\rangle \langle n|H_{e-ph}|m\rangle \langle m|H_{e-p}|i\rangle}{(E_{las} - E_m - i\Gamma_m)(E_{las} - E_n - i\Gamma_n)} \right|^2 \quad (9)$$

where  $\langle m|H_{e-p}|i\rangle$  and  $\langle f|H_{e-p}|n\rangle$  represent the electron-photon interaction processes, while  $\langle n|H_{e-ph}|m\rangle$  represents the electron-phonon interaction process. The terms  $|i\rangle$ ,  $|f\rangle$ ,  $|m\rangle$ , and  $|n\rangle$  are the initial, final, and two intermediate

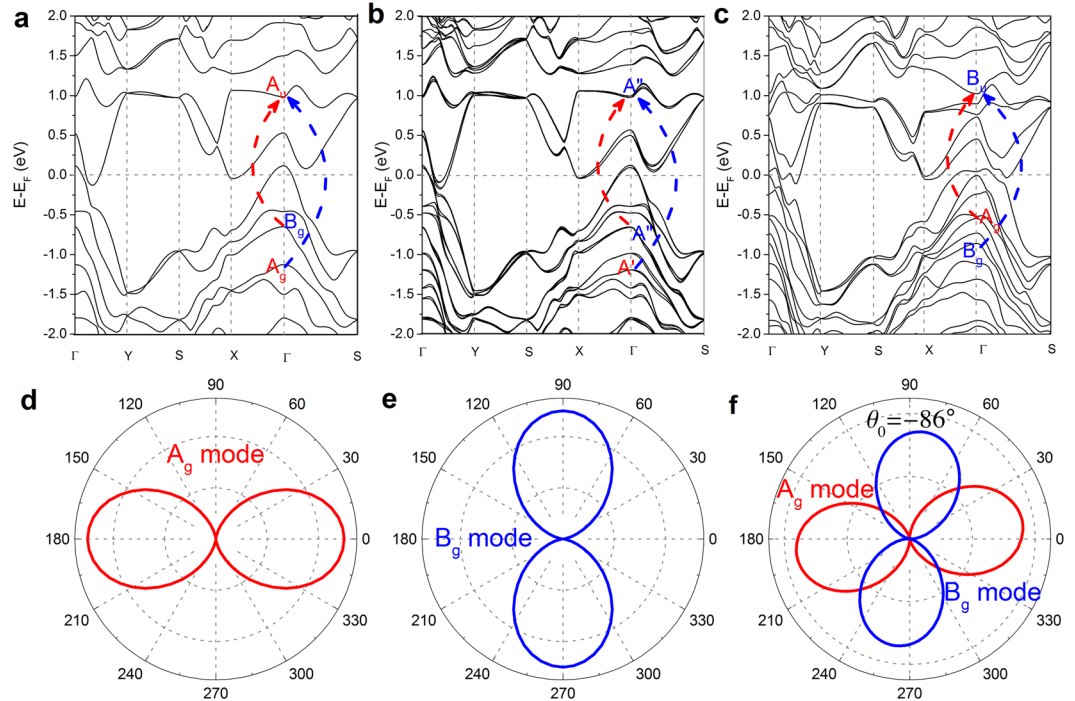


**Figure 5.** The density functional calculated band structure of (a) single-layer, (b) bilayer and (c) bulk 1 T' -MoTe<sub>2</sub>, the band symmetries in the Brillouin zone center  $\Gamma$  point are labeled, and  $A_g$  ( $A'$ ,  $A_u$ ) and  $B_g$  ( $A''$ ,  $B_u$ ) bands are indicated by red and blue labels, respectively. Calculated polarization dependence of the optical transition probability (d) with the maximum  $a$ -axis polarization ( $A_g$  mode) and (e) the maximum  $b$ -axis polarization ( $B_g$  mode). The  $0^\circ$  ( $90^\circ$ ) corresponds to the  $a$ -axis ( $b$ -axis) of the 1 T' -MoTe<sub>2</sub> sample. (f) Calculated polarization-dependence of the  $A_g$  and  $B_g$  phonon mode intensities, from the incident polarization rotation method.

states, respectively.  $E_m$  and  $E_n$  are the energies of the two intermediate states  $|m\rangle$  and  $|n\rangle$ .  $\Gamma_m$  and  $\Gamma_n$  are the damping constants related to the finite lifetimes of the two intermediate states. The electron-photon interaction contains the transition of the excited electron from the valence band to conduction band, protected by the optical selection rule. In order to explain the observed anisotropies of the Raman response in 1 T' -MoTe<sub>2</sub>, we performed electron-photon interaction calculations. We calculated the representative band structures of 1-layer, 2-layer, and bulk 1 T' -MoTe<sub>2</sub>. The symmetry of the eigen-function for each energy band at the  $\Gamma$  point was determined using first-principles calculations (Fig. 5a–c). If we neglect the polarization dependence of the electron-phonon matrix element  $\langle n|H_{e-ph}|m\rangle$ , the polarization dependence of the Raman intensity can be described by the product of two electron-photon matrix elements,  $\langle f|H_{e-p}|n\rangle$  and  $\langle m|H_{e-p}|i\rangle$ . In Raman scattering,  $H_{e-ph}$  selects the symmetry of  $|m\rangle$  and  $|n\rangle$ , while the initial  $|i\rangle$  and final  $|f\rangle$  states are the same. For the  $A_g$  ( $A'$ ) mode, the  $|m\rangle$  and  $|n\rangle$  states have the same symmetry, and the two electron-photon interaction matrix elements in equation (9) have the same polarization dependence ( $180^\circ$  period in the parallel-polarization by rotating the sample). On the other hand, the  $B_g$  ( $A''$ ) mode's  $|m\rangle$  and  $|n\rangle$  states have different symmetries, and the two matrix elements have the opposite polarization dependence that gives the  $90^\circ$  period. These are the optical transition selection rules which can be explained using group theory. The detailed selection rules for  $A_g$  ( $A'$ ) and  $B_g$  ( $A''$ ) Raman modes are summarized in supplementary Tables S2 and S3, respectively. Depending on the incident and scattered polarized light, we can excite  $A_g$  ( $A'$ ) phonon modes for  $aa$  and  $bb$  polarizations, and excite  $B_g$  ( $A''$ ) phonon modes for  $ab$  and  $ba$  polarizations. Here, we use the notation  $ab$  polarization to describe the Raman process with incident polarized light along  $a$ -axis and scattered polarized light along  $b$ -axis of the crystals. The other polarization conditions  $aa$ ,  $ba$ , and  $bb$  are defined accordingly.

For detailed analysis, we take the  $\Gamma$  point in single-layer 1 T' -MoTe<sub>2</sub> as an example. For  $E_{las} \approx 1.8$  eV, the transition between the  $B_g$  valence band and the  $A_u$  conduction band occurs when incident light polarization is along the  $a$ -axis. According to the symmetry selection rule, the polar plot of the transition probability with an incident light polarization rotation angle,  $\theta$ , shows a two-lobed shape (Fig. 5d), where the maximum absorption occurs when incident polarized light is long the  $a$ -axis. In the incident light polarization rotation method, since the scattered polarization is fixed, the photon emission process has no influence on the Raman intensity's polarization dependence<sup>28</sup>. When the scattered light polarization is along the  $a$ -axis ( $\theta_0 = 0^\circ$ ), this transition dispersion coincides with the calculated polarization-dependence of the  $A_g$  phonon mode's intensity. For  $E_{las} \approx 2.2$  eV, the transition between the  $A_g$  valence band and the  $A_u$  conduction band occurs when the incident polarized light is perpendicular to the crystalline  $a$ -axis. The polar plot of the transition probability coincides with the polarization-dependence of the  $B_g$  phonon mode (Fig. 5e), showing a two-lobed shape with maximum values when the incident light polarization is perpendicular to the crystalline  $a$ -axis. Similarly, the transition between the  $A''$  ( $A_g$ ) valence band and the  $A''$  ( $B_u$ ) conduction band occurs when incident polarized light polarization is along the  $a$ -axis for bilayer (bulk) 1 T' -MoTe<sub>2</sub>, while the transitions between the  $A'$  ( $B_g$ ) valence band and the  $A''$  ( $B_u$ ) conduction band occur when



incident polarized light is perpendicular to the  $a$ -axis for bilayer (bulk)  $1T'$ -MoTe<sub>2</sub>. For the case that the scattering light polarization is not parallel to the crystalline  $a$ -axis ( $\theta_0 \neq 0^\circ$ ), the representative polarization-dependence of the  $A_g$  and  $B_g$  phonon modes with  $\theta_0 = -86^\circ$  are calculated (Fig. 5f). These analytical results agree with our anisotropic experimental observations, but do not perfectly coincide with all the data points. For example, in the parallel polarization configuration, the formation of secondary maxima and non-zero minimum intensity in the  $A_g$  phonon modes cannot be completely explained by the anisotropic electron-photon interaction, revealing that the anisotropic electron-phonon interaction also contributes to its anisotropic Raman response.

## Conclusions

We systematically studied the anisotropic Raman response of monoclinic  $1T'$ -MoTe<sub>2</sub> from single layer to bulk using two different measurement methods. Through sample rotation method, the symmetries of the detected modes and the crystal orientation can be identified due to the different intensity variation periods. The thickness and excitation wavelength dependences of the anisotropic Raman response of  $1T'$ -MoTe<sub>2</sub> are carried out via rotating the incident polarization, while the sample orientation and scattered light polarization are fixed. Under this method, the polar plots of the intensities for all detected modes exhibit a two-lobed shape, while the main-axis orientations for different symmetric modes are different. Their polarization-dependent intensities roughly agree with the semi-classical model based on the Placzek approximation. Using the full quantum model based on the density functional and quantum perturbation theories, we demonstrate that the anisotropy of the Raman modes is influenced by both the anisotropic electron-photon interaction as well as the anisotropic electron-phonon interaction. Our research not only presents the in-plane anisotropic intensities of Raman modes in monoclinic 2D  $1T'$ -MoTe<sub>2</sub>, but also reveals the physical origin of the anisotropic Raman response, which is a crucial step to enable potential applications of  $1T'$ -MoTe<sub>2</sub> in novel electronic and optoelectronic devices where the anisotropic properties might be utilized.

## Methods

**Single-crystalline  $1T'$ -MoTe<sub>2</sub> growth.**  $1T'$ -MoTe<sub>2</sub> single crystals were grown via a chemical vapor transport (CVT) technique. Stoichiometric purified Mo (Sigma Aldrich 99.99%) and Te (Alfa Aesar 99.99%) powders were ground together and loaded into a quartz tube with a small amount of I<sub>2</sub> as the transport agent. The tube was sealed under vacuum, then placed and heated in a two-zone furnace. The hot and cold zones were kept at 1000 °C and 850 °C, respectively. After 10 days of growth, the  $1T'$ -MoTe<sub>2</sub> single crystals were obtained in the cold zone.

**Raman measurements.** The Raman measurements were carried out using a commercial micro-Raman system (Horiba Jobin Yvon HR800) under the backscattering geometry. A 100× object lens (NA = 0.85), and a 1800 grooves/mm grating were used in our measurements. The exposure time was 100 s. The laser power illuminated on the sample was below 400 μW to avoid the sample damage. All the measurements were carried out at room temperature.

**Density functional calculations.** The DFT calculations were carried out with the Vienna *ab-initio* Simulation Package (VASP)<sup>32</sup> based on density functional theory. The Perdew-Burke-Ernzerhof (PBE) exchange-correlation functional<sup>33</sup> along with the projector-augmented wave (PAW) potentials was employed for the self-consistent total energy calculations and geometry optimization. The kinetic energy cutoff for the plane wave basis set was chosen to be 500 eV for all calculation. The Brillouin zones were sampled using  $7 \times 14 \times 3$  (for bulk  $1T'$ -MoTe<sub>2</sub>) and  $7 \times 14 \times 1$  (for 1L-3L  $1T'$ -MoTe<sub>2</sub>) Monkhorst-Pack k-point grid. Atomic positions were relaxed until the energy differences were converged within  $10^{-5}$  eV and the maximum Hellmann-Feynman force on any atoms was below 0.01 eV/Å. We used a periodic supercell to simulate a 2D sheet, including a vacuum of 15 Å to separate the adjacent periodic images of the sheet. The spin-orbit interaction (SOC) was included in the calculation of electronic structure of bulk and few-layer  $1T'$ -MoTe<sub>2</sub>. The van der Waals (vdW) interactions were considered at the vdW-DF<sup>34,35</sup> level for geometry optimization, which was found to be more accurate in describing the structural properties of layered materials.

## References

- Mak, K. F., He, K., Shan, J. & Heinz, T. F. Control of valley polarization in monolayer MoS<sub>2</sub> by optical helicity. *Nature nanotechnology* **7**, 494–498, doi:10.1038/nnano.2012.96 (2012).
- Zeng, H. *et al.* Valley polarization in MoS<sub>2</sub> monolayers by optical pumping. *Nature nanotechnology* **7**, 490–493, doi:10.1038/nnano.2012.95 (2012).
- Cao, T. *et al.* Valley-selective circular dichroism of monolayer molybdenum disulfide. *Nature communications* **3**, 887, doi:10.1038/ncomms1882 (2012).
- Mak, K. F., McGill, K. L., Park, J. & McEuen, P. L. The valley Hall effect in MoS<sub>2</sub> transistors. *Science* **344**, 1489–1492, doi:10.1126/science.1250140 (2014).
- Mak, K. F. & Shan, J. Photonics and optoelectronics of 2D semiconductor transition metal dichalcogenides. *Nature Photonics* **10**, 216–226, doi:10.1038/nphoton.2015.282 (2016).
- Xia, F., Wang, H. & Jia, Y. Rediscovering black phosphorus as an anisotropic layered material for optoelectronics and electronics. *Nature communications* **5**, 4458, doi:10.1038/ncomms5458 (2014).
- Qiao, J. *et al.* High-mobility transport anisotropy and linear dichroism in few-layer black phosphorus. *Nature communications* **5**, 4475, doi:10.1038/ncomms5475 (2014).
- Luo, Z. *et al.* Anisotropic in-plane thermal conductivity observed in few-layer black phosphorus. *Nature communications* **6**, 8572, doi:10.1038/ncomms9572 (2015).
- Zhang, S. *et al.* Extraordinary Photoluminescence and Strong Temperature/Angle-Dependent Raman Responses in Few-Layer Phosphorene. *ACS Nano* **8**, 9590–9596, doi:10.1021/nn503893j (2014).
- Ribeiro, H. B. *et al.* Unusual Angular Dependence of the Raman Response in Black Phosphorus. *ACS Nano* **9**, 4270–4276, doi:10.1021/acsnano.5b00698 (2015).
- Wu, J. *et al.* Identifying the crystalline orientation of black phosphorus using angle-resolved polarized Raman spectroscopy. *Angewandte Chemie* **54**, 2366–2369, doi:10.1002/anie.201410108 (2015).
- Song, Q. *et al.* The In-Plane Anisotropy of WTe<sub>2</sub> Investigated by Angle-Dependent and Polarized Raman Spectroscopy. *Scientific reports* **6**, 29254, doi:10.1038/srep29254 (2016).

13. Qi, Y. *et al.* Superconductivity in Weyl semimetal candidate MoTe<sub>2</sub>. *Nature communications* **7**, 11038, doi:10.1038/ncomms11038 (2016).
14. Ali, M. N. *et al.* Large, non-saturating magnetoresistance in WTe<sub>2</sub>. *Nature* **514**, 205–208, doi:10.1038/nature13763 (2014).
15. Soluyanov, A. A. *et al.* Type-II Weyl semimetals. *Nature* **527**, 495–498, doi:10.1038/nature15768 (2015).
16. Kang, D. *et al.* Superconductivity emerging from a suppressed large magnetoresistant state in tungsten ditelluride. *Nature communications* **6**, 7804, doi:10.1038/ncomms8804 (2015).
17. Qian, X., L. J., Liang, F. & Li, J. Quantum spin Hall effect in two-dimensional transition metal dichalcogenides. *Science* **346**, 1344–1348, doi:10.1126/science.1256815 (2014).
18. Cho, S. *et al.* Phase patterning for ohmic homojunction contact in MoTe<sub>2</sub>. *Science* **349**, 625–629, doi:10.1126/science.aab3175 (2015).
19. Deng, K. *et al.* Experimental observation of topological Fermi arcs in type-II Weyl semimetal MoTe<sub>2</sub>. *Nature Physics* **12**, 1105–1110, doi:10.1038/nphys3871 (2016).
20. Pan, X. C. *et al.* Pressure-driven dome-shaped superconductivity and electronic structural evolution in tungsten ditelluride. *Nature communications* **6**, 7805, doi:10.1038/ncomms8805 (2015).
21. Cai, P. L. *et al.* Drastic Pressure Effect on the Extremely Large Magnetoresistance in WTe<sub>2</sub>: Quantum Oscillation Study. *Physical review letters* **115**, 057202, doi:10.1103/PhysRevLett.115.057202 (2015).
22. Keum, D. H. *et al.* Bandgap opening in few-layered monoclinic MoTe<sub>2</sub>. *Nature Physics* **11**, 482–486, doi:10.1038/nphys3314 (2015).
23. Zhou, L. *et al.* Large-Area Synthesis of High-Quality Uniform Few-Layer MoTe<sub>2</sub>. *Journal of the American Chemical Society* **137**, 11892–11895, doi:10.1021/jacs.5b07452 (2015).
24. Zhang, X. *et al.* Phonon and Raman scattering of two-dimensional transition metal dichalcogenides from monolayer, multilayer to bulk material. *Chemical Society reviews* **44**, 2757–2785, doi:10.1039/c4cs00282b (2015).
25. Song, Q. J. *et al.* Physical origin of Davydov splitting and resonant Raman spectroscopy of Davydov components in multilayer MoTe<sub>2</sub>. *Physical Review B* **93**, doi:10.1103/PhysRevB.93.115409 (2016).
26. Froehlicher, G. *et al.* Unified Description of the Optical Phonon Modes in N-Layer MoTe<sub>2</sub>. *Nano letters* **15**, 6481–6489, doi:10.1021/acs.nanolett.5b02683 (2015).
27. Chen, S. Y. *et al.* Activation of New Raman Modes by Inversion Symmetry Breaking in Type II Weyl Semimetal Candidate T'-MoTe<sub>2</sub>. *Nano letters* **16**, 5852–5860, doi:10.1021/acs.nanolett.6b02666 (2016).
28. Li, X. L. *et al.* Layer-Number Dependent Optical Properties of 2D Materials and Their Application for Thickness Determination. *Adv. Funct. Mater.* **2017**, 1604468, doi:10.1002/adfm.201604468 (2017).
29. Tan, Q. H. *et al.* Layer-number dependent high-frequency vibration modes in few-layer transition metal dichalcogenides induced by interlayer couplings. *Journal of Semiconductors* **2017**, 031006, doi:10.1088/1674-4926/38/3/031006 (2017).
30. Ling, X. *et al.* Anisotropic Electron-Photon and Electron-Phonon Interactions in Black Phosphorus. *Nano letters* **16**, 2260–2267, doi:10.1021/acs.nanolett.5b04540 (2016).
31. Kim, J. *et al.* Anomalous polarization dependence of Raman scattering and crystallographic orientation of black phosphorus. *Nanoscale* **7**, 18708–18715, doi:10.1039/c5nr04349b (2015).
32. Kresse, G. & J. F. Efficient iterative schemes for ab initio total-energy calculations using a plane-wave basis set. *PHYSICAL REVIEW B* **54**, 11169–11186, doi:10.1103/PhysRevB.54.11169 (1996).
33. Perdew, J. P. & Matthias Ernzerhof, K. B. Generalized Gradient Approximation Made Simple. *PHYSICAL REVIEW LETTERS* **77**, 3865–3868, doi:10.1103/PhysRevLett.77.3865 (1996).
34. Dion, M. *et al.* van der Waals density functional for general geometries. *Physical review letters* **92**, 246401, doi:10.1103/PhysRevLett.92.246401 (2004).
35. Lee, K. *et al.* Higher-accuracy van der Waals density functional. *Physical Review B* **82**, doi:10.1103/PhysRevB.82.081101 (2010).

## Acknowledgements

We acknowledge support from the National Key Projects for Basic Research Program of China (2013CB921901, 2012CB932703, 2013CB922103, and 2011CB922103), the National Natural Science Foundation of China (Grants nos. 61521004, 61125402, 61404003, 51172004, 11474007, 11225421, 11434010, 11474277, 91421109, 11134005, 61176088, 11522432, 11525417 and 11274003).

## Author Contributions

Q.S., Y.Y. and L.D. conceived the project and carried out the data analysis. X.P. and F.S. grew the bulk 1T'-MoTe<sub>2</sub> crystals. H.W., and X.W. performed the density functional theory calculations. Q.S. and X.X. performed the Raman measurements. Q.S., Y.W. and Y.L. performed the atomic force microscopy measurements. Q.S., Y.Y. and L.D. wrote the manuscript and all authors contributed to discussions.

## Additional Information

**Supplementary information** accompanies this paper at doi:10.1038/s41598-017-01874-2

**Competing Interests:** The authors declare that they have no competing interests.

**Change History:** A correction to this article has been published and is linked from the HTML version of this paper. The error has not been fixed in the paper.

**Publisher's note:** Springer Nature remains neutral with regard to jurisdictional claims in published maps and institutional affiliations.



**Open Access** This article is licensed under a Creative Commons Attribution 4.0 International License, which permits use, sharing, adaptation, distribution and reproduction in any medium or format, as long as you give appropriate credit to the original author(s) and the source, provide a link to the Creative Commons license, and indicate if changes were made. The images or other third party material in this article are included in the article's Creative Commons license, unless indicated otherwise in a credit line to the material. If material is not included in the article's Creative Commons license and your intended use is not permitted by statutory regulation or exceeds the permitted use, you will need to obtain permission directly from the copyright holder. To view a copy of this license, visit <http://creativecommons.org/licenses/by/4.0/>.

© The Author(s) 2017